Nonlinear Wave Growth Analysis of Whistler - Mode Chorus Generation Regions Based on Coupled MHD and Advection Simulation of the Inner Magnetosphere

AUTHOR(S):

Ebihara, Yusuke; Ikeda, Takuya; Omura, Yoshiharu; Tanaka, Takashi; Fok, Mei - Ching

AGU100 ADVANCING EARTH AND SPACE SCIENCE

JGR Space Physics

RESEARCH ARTICLE
10.1029/2019JA026951

Key Points:
- Coupled model is used to specify the region where whistler-mode chorus waves grow nonlinearly in the inner magnetosphere
- When solar wind speed is high, whistler waves grow more efficiently due to linear and nonlinear mechanisms over wide areas
- For slow solar wind, linear growth is mostly suppressed, but nonlinear wave growth still takes place with external seed waves

Correspondence to:
Y. Ebihara,
ebihara@rish.kyoto-u.ac.jp

Citation:
Ebihara, Y., Ikeda, T., Omura, Y., Tanaka, T., & Fok, M.-C. (2020). Nonlinear wave growth analysis of whistler-mode chorus generation regions based on coupled MHD and advection simulation of the inner magnetosphere. *Journal of Geophysical Research: Space Physics*, *125*, e2019JA026951. https://doi.org/10.1029/2019JA026951

Received 16 MAY 2019
Accepted 31 DEC 2019
Accepted article online 3 JAN 2020

Nonlinear Wave Growth Analysis of Whistler-Mode Chorus Generation Regions Based on Coupled MHD and Advection Simulation of the Inner Magnetosphere

Yusuke Ebihara[1], Takuya Ikeda[1], Yoshiharu Omura[1], Takashi Tanaka[2], and Mei-Ching Fok[3]

[1]Research Institute for Sustainable Humanosphere, Kyoto University, Uji, Japan, [2]International Center for Space Weather Science and Education, Kyushu University, Fukuoka, Japan, [3]NASA GSFC, Greenbelt, MD, USA

Abstract We show the regions where nonlinear growth of whistler-mode chorus waves is preferred to occur in the inner magnetosphere. A global magnetohydrodynamics (MHD) simulation was used to obtain large-scale electric and magnetic fields under the southward interplanetary magnetic field condition. With the electric and magnetic fields obtained by the MHD simulation, we ran a comprehensive inner magnetosphere-ionosphere model to solve the evolution of phase space density of electrons. Hot electrons originating from the tail region drift sunward and penetrate deep into the inner region due to a combination of convection and substorm-associated electric fields. Cold electrons also drift sunward, resulting in a contraction of the plasmasphere. We obtained the following results. (1) The whistler waves can first grow due to the linear mechanism (pitch angle anisotropy) in the premidnight-prenoon region outside the plasmapause, followed by rapid, nonlinear mechanism accompanied with rising-tone chorus elements. (2) When the solar wind speed is high, the whistler waves grow more efficiently due to linear and nonlinear mechanisms over a wider area because of deep penetration of hot electrons and the large contraction of the plasmasphere. This is consistent with the observation that the outer belt electrons increase for the fast solar wind. (3) For slow solar wind, the linear growth is mostly suppressed, but the nonlinear growth can still take place when external seed waves are present. This may explain the persistence of dawn chorus and large-amplitude chorus waves that are often observed in the premidnight-postdawn region in relatively weak geomagnetic activities.

1. Introduction

Whistler-mode chorus waves are intense, discrete electromagnetic emissions in the VLF range, which are often observed outside the plasmapause in the morning magnetosphere (Burtis & Helliwell, 1969, 1976; Tsurutani & Smith, 1974). Statistical studies have shown that the wave amplitude increases with the auroral electrojet (*AE*) index with magnetic local time (MLT) centered in the postmidnight sector (Meredith et al., 2003). The highest amplitude of the chorus waves is distributed in the region $4 < L < 6$ from 0300 and 1000 MLT. The chorus waves are sometimes accompanied with rising tones, in which frequency of the wave increases monotonically (Santolík et al., 2003).

With quasilinear theory for the generation of the whistler waves proposed by Kennel and Petschek (1966), Jordanova et al. (2010) have solved a four-dimensional advection equation for trapped electrons and have shown the global distribution of the linear growth rate of the chorus wave. Hot electrons with energy of 1–30 keV propagate earthward due to the enhanced dawn-dusk electric field. Due to pitch angle anisotropy of the newly injected hot electrons, intense whistler-mode waves are shown to grow outside the plasmasphere ($L > 4$) in the premidnight to dawn sector. This is consistent with observations (Meredith et al., 2003). It has been suggested that when the wave amplitude reaches a certain threshold, coherent chorus waves grow efficiently due to a nonlinear effect (Hikishima et al., 2009; Katoh & Omura, 2007; Nunn, 1974; Omura et al., 2008; Roux & Pellat, 1978; Trakhtengerts, 1995). As the wave grows at a frequency of the largest linear growth rate, the wave becomes coherent suppressing the growth of other waves around the frequency. Once the wave amplitude exceeds a threshold amplitude for an absolute nonlinear instability, the wave amplitude grows with frequency increasing monotonically at the equator (Omura et al., 2009). The nonlinear wave growth stops near the optimum wave amplitude (Omura & Nunn, 2011) and then decreases

gradually to the level of the threshold amplitude, resulting in a short subpacket of a chorus wave element. The subpacket propagates away from the equator interacting with counter streaming resonant electrons in the downstream of the wave propagation. The gyro-phases of the resonant electrons are modulated by the wave with frequencies higher than that of the original triggering wave. The phase-modulated resonant electrons generate a new wave with the higher frequency in the upstream from the equator. The new wave triggers another cycle of the nonlinear wave growth, which is repeated to produce successive subpackets. Through the repetition of the subpacket formation, the wave frequency gradually increases forming a rising-tone chorus element consisting of a series of subpackets.

The importance of resonant interaction of electrons with the whistler-mode chorus waves has been suggested in the generation of diffuse aurora (pulsating aurora) (Cornwall et al., 1970; Davidson, 1979; Rosenberg et al., 1971, 1981), loss of energetic electrons (Cornwall, 1964; Davidson & Walt, 1977; Dungey, 1963; Kennel & Petschek, 1966; Lyons et al., 1972; Rosenberg et al., 1971; Spjeldvik & Thorne, 1975), and rebuilt of the outer radiation belt (Horne & Thorne, 1998; Summers et al., 1998; Summers & Ma, 2000). Recent in situ observations show one-to-one correspondence between chorus waves and pulsating patches (Nishimura et al., 2010), magnetospheric electrons and pulsating patches (Jaynes et al., 2013), and chorus waves, electrons inside the loss cone, and pulsating patch (Kasahara et al., 2018). A good correlation between chorus elements (riser) and electron precipitation has been obtained on the basis of ground observations (Foster & Rosenberg, 1976; Rosenberg et al., 1971). The coherent chorus waves have been suggested to scatter and accelerate electrons more efficiently due to nonlinear cyclotron resonant interaction (Albert, 2002; Bortnik et al., 2008; Kubota & Omura, 2018; Omura et al., 2007, 2015, 2019; Summers & Omura, 2007). Note that the nonlinear interaction between the chorus waves and particles is different from the linear one. Diffusion taking place in momentum space is considered in the quasilinear theory (Lyons, 1974; Summers et al., 1998), whereas nondiffusive processes, such as phase trapping, are involved in the nonlinear theory (Omura et al., 2015).

The purpose of this study is to specify, for the first time, the regions where the nonlinear chorus waves are preferred to grow in the inner magnetosphere. The nonlinear wave growth theory that we used in the present study is based on a nonlinear growth rate obtained by assuming formation of an electromagnetic electron hole in the velocity phase space and its deformation due to the frequency variation and the spatial inhomogeneity of the background magnetic field (Omura et al., 2008). Associated with the nonlinear wave growth process, we calculated the threshold and optimum wave amplitudes that have also been derived by Omura et al. (2009) and Omura and Nunn (2011). A number of nonlinear theories have been suggested on the wave growth process (Nunn, 1974; Roux & Pellat, 1978; Trakhtengerts, 1995; Vomvoridis et al., 1982). While these theories basically assume nonlinear trajectories of resonant particles, the models and assumptions for the nonlinear growth rates are different from those used by Omura et al. (2009) and Omura and Nunn (2011). A global magnetohydrodynamic (MHD) simulation is used to determine self-consistently the global magnetic field and the electric field. We also solve a four-dimensional advection equation to obtain the phase space density of trapped electrons (hot electrons) with energy from ~keV to ~MeV under the electric and magnetic fields obtained by the global MHD simulation. The evolution of the cold electron density is also solved. Finally, we calculated the linear and nonlinear growth rates in the equatorial plane in the inner magnetosphere in response to different solar wind conditions.

2. Methods

2.1. Global MHD Simulation

The global MHD simulation REPPU (REProduce Plasma Universe) (Tanaka, 2015) is used to specify the magnetic and electric fields. REPPU employs a grid system based on triangular prisms. A sphere at the inner boundary (2.6 R_E) is first divided into 12 pentagons. We further divide each pentagon into five triangles and obtain 60 triangles in total (Level 1). Dividing each triangle into four, we obtain 240 triangles (Level 2). We use Level 6, in which a sphere is divided into 61,440 triangles, and stack 320 triangular prisms outward from the inner boundary. The outer boundary of the simulation domain is located at 200 R_E at midnight and 600 R_E at noon. The region between 1 and 2.6 R_E is not solved by REPPU, but the ionosphere is coupled with the magnetosphere in the manner described below. After mapping the field-aligned current and the plasma pressure in the inner boundary of the simulation domain to the ionosphere, we calculate the ionospheric

Table 1
IMF B_z Used for the Boundary Condition of the MHD Simulation

Time T (min)	IMF B_z (nT)
From −480 to −300	5
From −300 to −180	−5
From −180 to 0	5
From 0 onward	−5

conductivity. Second, we obtain an electric potential in the ionosphere Φ_i by solving a partial differential equation, and impose the electric field to the inner boundary of the simulation domain. Readers may refer to Ebihara et al. (2014) for detailed information about the calculation of the ionospheric conductivity. Many substorm-associated phenomena that are observable in the ionosphere and the magnetosphere are known to be reproduced by REPPU. They include, for example, auroral electrojets (Ebihara et al., 2019; Takashi Tanaka, 2015) Joule dissipation rates (Ebihara et al., 2019), a westward traveling surge (Ebihara & Tanaka, 2015a; Tanaka, 2015), and counter electrojet at the magnetic equator (Ebihara et al., 2014), earthward fast flow in the plasma sheet (Tanaka et al., 2017), dipolarization in the near-Earth magnetosphere (Tanaka et al., 2017), generation of field-aligned currents directly related to substorm expansion (Ebihara & Tanaka, 2015a, 2015b; Tanaka, 2015).

We impose the following solar wind parameters on the outer boundary of the MHD simulation. The y component of the IMF (IMF B_y) is held constant to be −2.5 nT, whereas the z component of the IMF (IMF B_z) is changed as shown in Table 1. The solar wind speed is changed as shown in Table 2. At $T = 0$, the solar wind speed increases to 1,000 km/s for Run 1 (fast solar wind case), whereas it remains to be 400 km/s for Run 2 (slow solar wind case). The solar wind density is held constant to be 2.5 cm^{-3}. The magnetosphere is expected to achieve quasi-steady state by $T = 0$.

2.2. Advection of Trapped Electrons

A comprehensive inner magnetosphere-ionosphere (CIMI) model is used to solve an advection equation for phase space density of trapped electrons (Fok et al., 2014). The phase space density f is specified by four parameters, the geomagnetic latitude (MLAT) λ_i, the MLT ϕ_i, M, and K. M is the first adiabatic invariant, being $p_\perp^2/2m_0B$, where $p_\perp$ is the moment in the perpendicular direction, and m_0 is rest mass. $K = J\sqrt{8m_0M}$, where J is the second invariant (Roederer, 1970). The subscript i implies a quantity at the ionospheric altitude. Position space (λ_i and ϕ_i) is fixed at the ionospheric altitude. The advantage of the use of position space fixed at the ionospheric altitude is that the equatorial plane is not necessary to be a plane. The equatorial plane (minimum B plane) can be warped by the magnetospheric current systems. The original version of CIMI takes into account pitch angle diffusion, energy diffusion, and cross diffusion. We exclude all the diffusion terms and we solve the equation as

$$\frac{\partial f}{\partial t} + \dot{\lambda}_i \frac{\partial f}{\partial \lambda_i} + \dot{\phi}_i \frac{\partial f}{\partial \phi_i} = -\left(\frac{f}{0.5\tau_b}\right)_{\text{Loss cone}} \tag{1}$$

where τ_b is the bounce period of the electrons. The operator denotes the bounce-averaged value. The hot electron density N_h is calculated by

$$N_h = \int f d\mathbf{p}. \tag{2}$$

CIMI also solves the evolution of cold electron density N_c as

$$\frac{\partial N_c}{\partial t} + \dot{\lambda}_i \frac{\partial N_c}{\partial \lambda_i} + \dot{\phi}_i \frac{\partial N_c}{\partial \phi_i} = \frac{F_n + F_s}{B_i} \tag{3}$$

where B_i is the strength of the magnetic field at the ionosphere altitude and F_n and F_s are the upward flux of cold electrons supplied from the ionosphere in the Northern Hemisphere and the Southern Hemisphere.

The three-dimensional distribution of the magnetic field provided by REPPU is used for calculation of the bounce-averaged magnetic drift (including the curvature and the grad-B drift) velocity. The ionospheric electric field determines the bounce-averaged E × B drift velocity. CIMI starts solving the advection equation at $T = 0$. The initial condition of f is given by a combination of the empirical model AE8 (Vette, 1991) and the kappa distribution (Xiao et al., 1998) with density of 0.01 cm^{-3}, characteristic energy of 1 keV, and κ of 4. At the outer boundary, we impose the kappa distribution with density of 0.5 cm^{-3}, characteristic energy of 1 keV, and κ of 4. The pitch angle distribution at the boundary is assumed to be isotropic. At the inner boundary, f is given to be zero. The outer and inner boundaries of the simulation domain of CIMI are located at 66.0°

Table 2
Solar Wind Speed Used for the Boundary Condition of the MHD Simulation

Time T (min)	Solar wind speed (km/s)	
From −480 to 0	400	
From 0 onward	1,000 (Run 1)	400 (Run 2)

and 8.7° MLAT, respectively, at the ionospheric altitude. The phase space density in the *M-K* space is converted to the energy-equatorial pitch angle space. The primary output of CIMI is the phase space density of hot electrons f from ~1 keV to ~4 MeV with all pitch angles.

2.3. Linear Wave Growth Rate

From the dispersion relation of the whistler-mode wave, the resonance velocity is given by (Omura et al., 2013)

$$V_R = c\left(\frac{1}{1+\xi^2}\right)^{1/2}\left(1-\frac{\Omega_e}{\gamma\omega}\right), \tag{4}$$

where

$$\xi = \frac{[\omega(\Omega_e-\omega)]^{1/2}}{\omega_{pe}}, \tag{5}$$

c, γ, ω, Ω_e, and ω_{pe} are the speed of light, the Lorentz factor, the wave frequency, the electron cyclotron frequency, and the electron plasma frequency, respectively. The cyclotron frequency and the electron plasma frequency are given by

$$\Omega_e = \frac{eB}{m_e} \tag{6}$$

and

$$\omega_{pe} = \sqrt{\frac{e^2N}{\varepsilon_0 m_e}}, \tag{7}$$

respectively. e is the elementary charge, m_e is the rest mass of the electron, N is electron density, ε_0 is the electric constant, and γ is given by

$$\gamma = \frac{1}{\sqrt{1-(v/c)^2}}, \tag{8}$$

where v is the speed of electron. For relativistic case, the linear growth rate of the whistler-mode wave Γ_L is given by (Xiao et al., 1998)

$$\Gamma_L = \frac{\pi {\omega_{pe}}^2 \eta_{rel}}{2\omega + \omega_{pe}^2\Omega_e/\left(\omega-\Omega_e^2\right)^2}(A_{rel}-\beta) \tag{9}$$

where

$$A_{rel} = \frac{\frac{k}{\omega-\Omega_e}\int_0^\infty \frac{dp_\perp}{\Delta_R}\frac{p_\perp^2}{\gamma_R}\left[p_\perp\frac{\partial f_1}{\partial p_\parallel}-p_\parallel\frac{\partial f_1}{\partial p_\perp}\right]_{p_\parallel=p_R}}{\int_0^\infty \frac{dp_\perp}{\Delta_R}p^2{}_\perp\left[\frac{\partial f_1}{\partial p_\perp}\right]_{p_\parallel=p_R}}, \tag{10}$$

$$\eta_{rel} = \pi v_h \frac{\omega-\Omega_e}{k}\int_0^\infty \frac{p_\perp^2 dp_\perp}{\Delta_R}\left[\frac{\partial f_1}{\partial p_\perp}\right]_{p_\parallel=p_R}, \tag{11}$$

and

$$\beta = \frac{1}{\Omega_e/\omega-1}, \tag{12}$$

and

$$\Delta_R = 1 - \frac{\omega p_R}{c^2 k \gamma_R}. \tag{13}$$

Here ω is the wave frequency, k is the wave number derived from dispersion relation, p is the momentum, ν_h is the ratio of the hot electron density to the cold electron density, and f_1 is the phase space density of hot electrons divided by the cold electron density. A_{rel} implies pitch angle anisotropy. p_R and γ_R are the resonant values of the electron parallel momentum and the Lorentz factor, respectively.

2.4. Nonlinear Wave Growth Rate

The nonlinear growth rate of the whistler-mode chorus emission is calculated on the basis of the theory provided by Omura et al. (2013). The nonlinear wave growth theory is based on the nonlinear motions of resonant electrons approximated by those of electrons with the average perpendicular velocity $V_{\perp 0}$, which is also used for calculation of the resonant currents modifying the wave frequency and amplitude. With this approximation, the nonlinear growth rate of the whistler-mode chorus wave is given by

$$\Gamma_N = \frac{Q\omega_{ph}^2}{2}\left(\frac{\xi}{\omega\Omega_w}\right)^{1/2}\frac{V_g}{U_{t\parallel}}\left(\frac{\chi V_{\perp 0}}{c\pi\gamma}\right)^{3/2}\exp\left(-\frac{\gamma^2 V_R^2}{2{U_{t\parallel}}^2}\right), \tag{14}$$

where

$$\chi^2 = \frac{1}{1+\xi^2}, \tag{15}$$

$$\omega_{ph} = \sqrt{\frac{N_h e^2}{\varepsilon_0 m_e}}, \tag{16}$$

and

$$V_g = \frac{c\xi}{\chi}\left[\xi^2 + \frac{\Omega_e}{2\Omega_e - \omega}\right]^{-1}. \tag{17}$$

The parameter $U_{t\parallel}$ is the thermal momentum per unit mass in the parallel direction and N_h is the hot electron density. The parameter Q represents the depth of the electron hole generated by trapped resonant electrons (Omura et al., 2009), which is assumed to be 0.5. The parameter Ω_w is the normalized wave amplitude, V_g is the group velocity of the wave, and k is the wave number. The wave amplitude B_w is assumed to be 0.01% of the magnitude of the local magnetic field (Santolík et al., 2004).

The temporal growth rate must be positive to emit chorus waves at equator. This condition is satisfied when $\Omega_\mathrm{w} > \Omega_\mathrm{th}$, where Ω_th is the threshold wave amplitude (Omura et al., 2009) for the nonlinear wave growth. The threshold wave amplitude is given by

$$\frac{\Omega_{th}}{\Omega_e} = \frac{100\pi^3\gamma^3\xi}{\widetilde{\omega}\widetilde{\omega}_{ph}^4\widetilde{V}_{\perp 0}^5\chi^5}\left(\frac{\widetilde{a}s_2\widetilde{U}_{t\parallel}}{Q}\right)^2\exp\left(\frac{\gamma^2\widetilde{V}_R^2}{\widetilde{U}_{t\parallel}^2}\right), \tag{18}$$

where $\widetilde{V}_{\perp 0} = V_{\perp 0}/c$, $\widetilde{\omega} = \omega/\Omega_e$, $\widetilde{a} = ac^2/\Omega_e^2$, $\widetilde{U}_{t\parallel} = U_{t\parallel}/c$, and $\widetilde{\omega}_{ph} = \omega_{ph}/\Omega_e$.

$$s_2 = \frac{1}{2\xi\chi}\left\{\frac{\gamma\omega}{\Omega_e}\left(\frac{V_{\perp 0}}{c}\right)^2 - \left[2 + \Lambda\frac{\chi^2(\Omega_e - \gamma\omega)}{\Omega_e - \omega}\right]\frac{V_R V_p}{c^2}\right\}, \tag{19}$$

and

$$V_p = \frac{\omega}{k} = c\chi\xi. \tag{20}$$

We assume that $\Lambda = \omega/\Omega_e$ (Omura et al., 2009). The parameter a represents magnetic inhomogeneity (Omura et al., 2009), which is given by

$$a = \frac{1}{h^2}\left(\frac{B(h)}{B_0} - 1\right), \tag{21}$$

where h is a small distance along a magnetic field line from the equatorial plane and B_0 is the magnetic field in the equatorial plane. For this particular study, we use h of 0.2 R_E to calculate the parameter a.

When the wave amplitude is higher than the optimum wave amplitude Ω_{opt}, rising-tone chorus elements are emitted (Omura & Nunn, 2011). The optimum wave amplitude is given by

$$\frac{\Omega_{opt}}{\Omega_e} = 0.81\pi^{-5/2}\frac{Q}{\tau}\frac{s_1\widetilde{V}_g}{s_0\,\widetilde{\omega}\,\widetilde{U}_{t\|}}\left(\frac{\chi\widetilde{\omega}_{ph}\widetilde{V}_{\perp 0}}{\gamma}\right)^2 \exp\left(-\frac{\gamma^2\widetilde{V}_R^2}{2\widetilde{U}_{t\|}^2}\right), \tag{22}$$

where

$$s_0 = \frac{\chi}{\xi}\frac{V_{\perp 0}}{c}, \tag{23}$$

and

$$s_1 = \gamma\left(1 - \frac{V_R}{V_g}\right)^2. \tag{24}$$

We assume that $\tau = 0.5$ based on observations (Kurita et al., 2012). The parameters $V_{\perp 0}$ and $U_{t\|}(=\gamma V_{t\|})$ are given by

$$V_{\perp 0} = \frac{\int v_\perp F_1 d^3\mathbf{v}}{\int F_1 d^3\mathbf{v}} \tag{25}$$

and

$$V_{t\|}^2 = \frac{\int v_\|^2 F_1 d^3\mathbf{v}}{\int F_1 d^3\mathbf{v}}, \tag{26}$$

where F_1 is the velocity distribution function of the hot electrons obtained by CIMI.

3. Results

3.1. Large-Scale Electric Field

We turned IMF B_z southward at $T = 0$ upwind of the magnetosphere. The southward IMF reached the subsolar point of the magnetosheath at T ~7 min (Run 1, fast solar wind) and T ~12 min (Run 2, slow solar wind). Figure 1 summarizes electric potential at the ionosphere altitude at $T = 0$, 30, 60, and 90 min. A two-cell pattern of the electric potential, which resembles the DP2 current system (Nishida et al., 1966), is evident when the magnetosphere is exposed to the southward IMF. The two-cell pattern of the electric potential, a positively charged cell on the dawnside and a negatively charged one on the duskside, gives rise to the dawn-dusk electric field in the inner magnetosphere. The magnitude of the electric potential is obviously larger for Run 1 than for Run 2. The ionospheric electric field is used to calculate the E × B drift velocity of the hot and cold electrons trapped in the inner magnetosphere. Note that the ionospheric electric field is basically regarded as a potential field. CIMI can implicitly take into account the E × B drift of magnetospheric particles due to the inductive electric field (Fok et al., 2011). The reason is as follows. The coordinate system of CIMI is fixed at the ionosphere where the plasma beta is extremely low, so that the

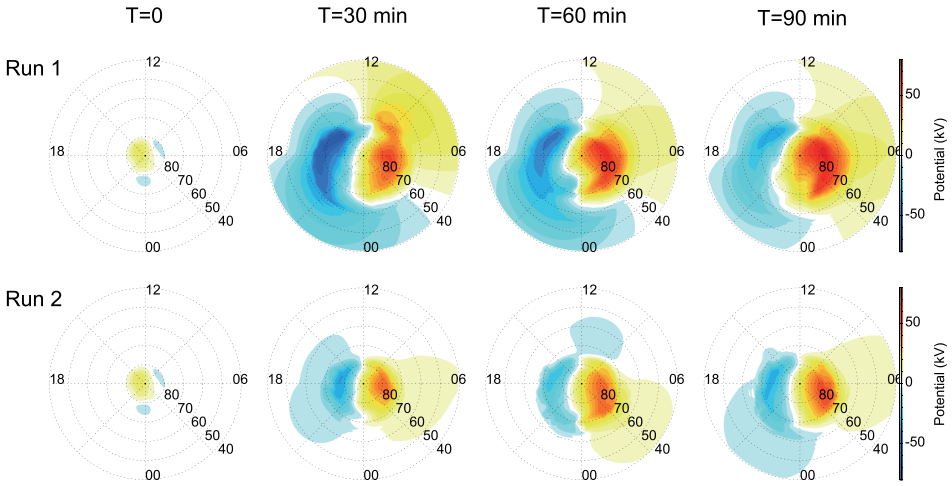

Figure 1. Simulated ionospheric electric potential in the MLT-MLAT coordinates at $T = 0$, 30, 60, and 90 min for Runs 1 (top) and 2 (bottom). The outer circle corresponds to 40 MLAT ($L = 1.7$).

induction electric field is supposed to be zero at the ionosphere. In the magnetosphere, when the resistivity is zero along a field line and the concept of frozen-in is valid, the induction electric field $\mathbf{E}_i$ ($= -\mathbf{V}_t \times \mathbf{B}$) is thought to be generated as the magnetic field changes, where $\mathbf{V}_t$ is the speed of plasma following the magnetic field. All the particles undergo the E × B drift in accordance with $\mathbf{E}_i$. For detailed explanation, readers may refer to Fok et al. (2011). Of course, grad-B and curvature drift of electrons is incorporated in CIMI in accordance with the instantaneous magnetic field provided by REPPU.

3.2. Auroral Electrojet and Penetration of Hot Electrons

Figure 2 shows the calculated auroral electrojet activity index *AE* (Davis & Sugiura, 1966), which is widely used to estimate the strength of the auroral electrojet. The *AE* index ($=AU - AL$) is calculated based on the variation of the *H*-component of the ground magnetic field taken at different MLTs at 67° MLAT. For Run 1, *AL* starts to show an abrupt negative excursion when the fast solar wind arrives at the magnetosphere, which is regarded a substorm associated with a shock. Since then, the *AL* has been less than −500 nT with some irregular fluctuations. Usually, a cycle of a substorm is characterized by a negative excursion of *AL* (Akasofu, 1968), but it is difficult to identify each substorm from the *AL* variations for Run 1. REPPU is also capable of reproducing many aspects of a substorm other than the *AL* variations as summarized in section 2.1.

The differential flux of electrons with 15 keV with equatorial pitch angle of 81° is also shown in Figure 2. As the electrons are transported to low *L* values, they are accelerated so as to conserve the first two adiabatic invariants. For Run 1 (fast solar wind case), the inner boundary of the newly penetrated electron population reaches $L = 3.7$ at $T = 90$ min. It is interesting to note that the electrons keep penetrating earthward whereas *AL* gradually increases (recovers) during the period from *T* ~60 to ~80 min. This implies that the deep penetration of the hot electrons is not only caused by substorm-associated electric field but also the large-scale convection electric field shown in Figure 1. For Run 2 (slow solar wind case), when the southward IMF reached the magnetosphere, *AL* starts to decreases gradually for ~40 min, corresponding to a substorm growth phase. The electrons penetrate to lower *L* value gradually due to the large-scale convection electric field. *AL* decreases abruptly at $T = 52$ min, corresponding to the beginning of the substorm expansion phase. The inner boundary of the newly injected electrons keeps penetrating earthward, whereas *AL* shows gradual increase (recovery) during the interval from $T = 75$ to 90 min. The inner boundary of the newly injected electrons reaches $L = 4.7$ at $T = 90$ min. Hereinafter, we focus on this moment ($T = 90$ min). The *AE* and *AL* values at $T = 90$ min are 1,064 and −908 nT for Run 1 (fast solar wind) and 321 and −242 nT for Run 2 (slow solar wind), respectively. The simulation results presented in this paper are obtained for the ideal, steady solar wind condition. When realistic solar wind variation is imposed to the REPPU code, the simulated *AE* values and the Joule dissipation rates in the ionosphere are in good agreement with observations (Ebihara et al., 2019).

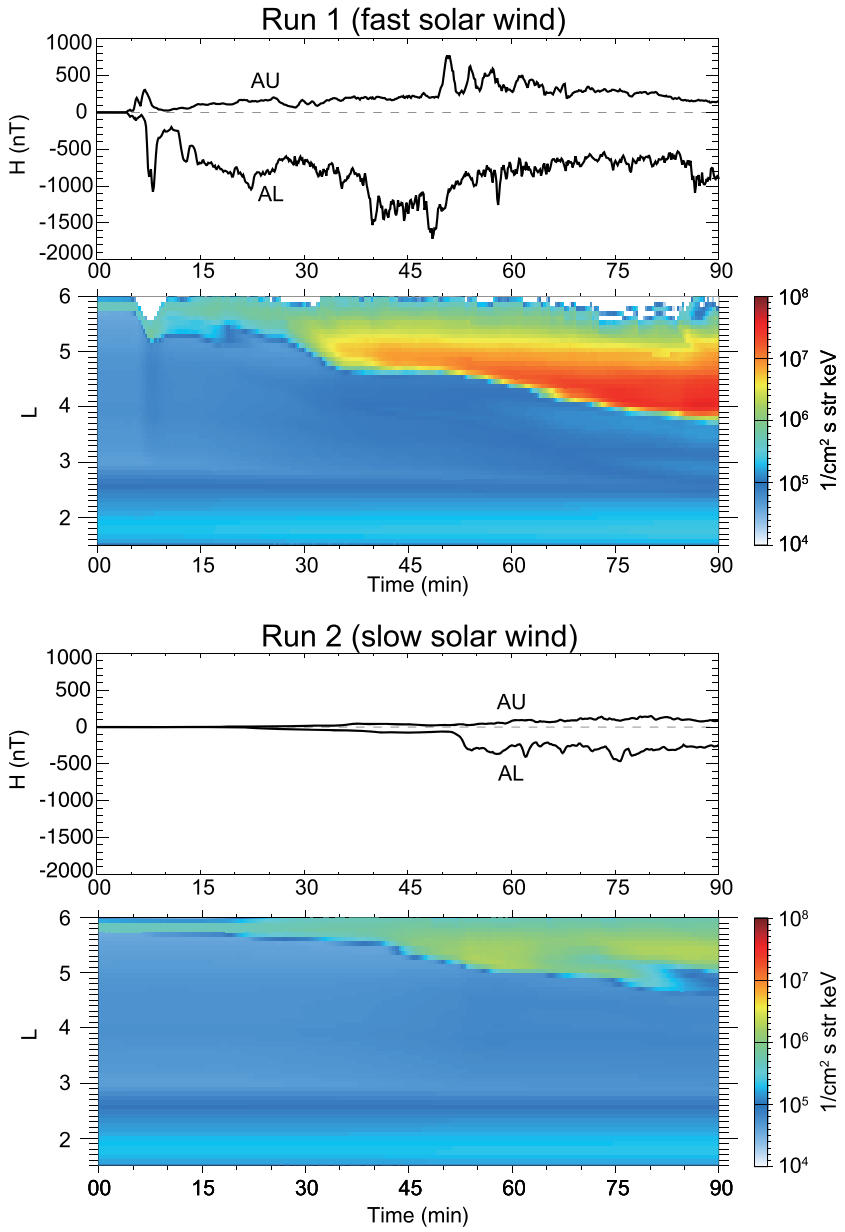

Figure 2. Simulated *AU* and *AL* indices and differential flux of electrons with energy 15 keV and equatorial pitch angle of 81° as a function of *L* and time at midnight for Runs 1 (fast solar wind) and 2 (slow solar wind).

3.3. Electron Densities, Pitch Angle Anisotropy, and Magnetic Field

Figure 3 summarizes the number density of cold electrons N_c, the number density of hot electrons N_h, pitch angle anisotropy A_{rel}, and the strength of the magnetic field in the equatorial plane at $T = 90$ min. The hot and cold densities are calculated by equations ((2)) and ((3)), respectively. The cold electrons that preexist in the inner magnetosphere drift sunward due to the enhanced convection electric field, resulting in a contraction of the plasmasphere. The plasmasphere is smaller for Run 1 (fast solar wind) than for Run 2 (slow solar wind) because the convection electric field for Run 1 is stronger than for Run 2. Hot electrons originating in the nightside boundary (tail region) penetrate deeper into the inner region for Run 1 than for Run 2. The inner edge of the penetrating hot electrons closely coincides with the outer edge of the plasmasphere. The coincidence can be understood in terms of a last-closed equipotential line or a forbidden region (Cowley & Ashour-Abdalla, 1976; Ejiri, 1978). Figure 14 of Ejiri et al. (1980) clearly demonstrates the inner

boundaries of the penetrating ions and electrons as a function of energy and L. The inner boundary of the electrons closely coincides with the theoretical location of the plasmapause indicated by a letter "P" in Figure 14 of Ejiri et al. (1980). The pitch angle anisotropy A_{rel} depends on wave frequency as indicated by (10). Here we plot A_{rel} at the wave frequency where the maximum linear growth rate occurs. Obviously, A_{rel} increases largely, in particular, near the leading edge of the newly injected electrons. The magnetic field shows day-night asymmetry. On the dayside, the magnetosphere is largely compressed by the solar wind. On the nightside, the magnetic field is stretched. The day-night asymmetry is greater for Run 1 than for Run 2.

3.4. Linear and Nonlinear Wave Growth

Figure 4 summarizes some quantities related to the wave growth at $T = 90$ min. For Run 1 (fast solar wind case), major features can be summarized as follows.

1. We seek the maximum value of the linear growth rate Γ_L of the whistler-mode wave at each position by varying wave frequency ω from $0.01\Omega_e$ to $0.99\Omega_e$. The maximum linear growth (MLG) rate normalized to local cyclotron frequency (Figure 4a) increases to 10^{-3}–10^{-2} on average at $L = 4$–5 in the premidnight-prenoon region. This is consistent with the simulation result obtained by Jordanova et al. (2010). The MLG rates occur at wave frequencies of ~$0.4\Omega_e$ (Figure 4b) at $L = 4$–5 in the premidnight-prenoon region. High-MLG rates are found in the region where both hot electron density and pitch angle anisotropy A_{rel} are high (Figure 3).
2. When the wave amplitude reaches the threshold amplitude Ω_{th} (equation (18)), the whistler-mode waves are expected to grow nonlinearly (onset of the nonlinear growth). The threshold amplitude at frequency of MLG (Figure 4c) significantly decreases and is lower than the optimum amplitude (Figure 4d) in the region where the linear growth rate is high. This implies that the whistler-mode waves grow due to the nonlinear processes with high growth rates (Figure 4e). The maximum nonlinear growth rate at the frequency of the MLG is ~4×10^{1} (Figure 4e), which is ~3–4 orders of magnitude higher than the linear one (Figure 4a).
3. We seek the maximum optimum amplitude (MOA) (equation (22)) by varying wave frequency ω. The MOA takes place at ~$0.6\Omega_e$ (Figure 4f). The MOA (Figure 4g) increases largely in the premidnight-prenoon region, indicating that the whistler waves can grow largely. At the frequency of the MOA, the nonlinear growth rate Γ_N for optimum amplitude (Figure 4h) reaches ~2×10^{-2} at L ~4.0–5.0 in the premidnight-prenoon region, which is comparable to, or ~1 order of magnitude higher than that of the linear growth rate. The nonlinear growth rate Γ_N (Figure 4 h) divided by the group velocity of the chorus wave is related to the convective growth. This means that the wave amplitude increases as the wave propagates from the equatorial plane (Omura et al., 2013). The nonlinear growth rate Γ_N at the MOA (Figure 4h) is found be high in the premidnight to prenoon region, implying that the chorus waves grow efficiently as they propagate from the equatorial plane. The whistler waves can be excited at various frequencies in the course of the nonlinear growth (Hikishima et al., 2009). When some of the coherent waves, including those coming from external sources, are present at the frequency of the MOA, the waves are expected to trigger chorus waves nonlinearly (Omura et al., 2015).

For Run 2 (slow solar wind case), major features of the simulation results are summarized as follows.

1. The normalized MLG rate (Figure 4i) is ~4×10^{-4} in the midnight-dawn sector, which is much lower than for Run 1 (fast solar wind case). The MLG occurred at ~$0.4\Omega_e$ (Figure 4j).
2. The optimum amplitude is higher than the threshold amplitude (that is, $\Omega_{opt} > \Omega_{th}$) (Figure 4l), meaning that the whistler-mode waves can grow nonlinearly at the frequency of the MLG. The nonlinear growth rates at the frequency of the MLG (Figure 4m) are extremely lower than for Run 2.
3. The optimum amplitude (Figure 4o) and the nonlinear growth rates for the optimum amplitude (Figure 4p) are also high at the wave frequency of the MOA. However, they are smaller, and less extensive than for Run 1.

Figure 5 summarizes the number densities (N_h and N_c), the pitch angle anisotropy A_{rel} at wave frequency where the maximum linear growth rate occurs, and the normalized growth rates as a function of L at midnight at $T = 90$ min. For Run 1 (left panels), the cold electron density (top panel) decreases with L abruptly at L ~3.6, which can be regarded as the plasmapause. The hot dense electrons increase at $L > 3.6$, which originate from the nightside boundary (tail region). The inner edge of the hot dense electrons nearly coincides

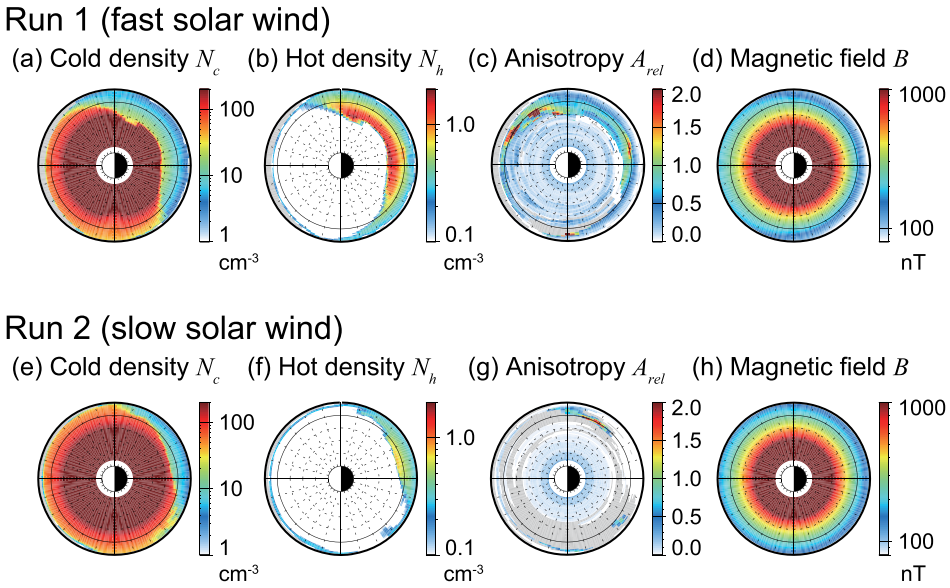

Figure 3. From left to right, number density of cold electrons N_c, number density of hot electrons N_h, pitch angle anisotropy A_{rel} at the wave frequency where the maximum linear growth rate occurs, and magnetic field B in the equatorial plane at $T = 90$ min for Runs 1 (top) and 2 (bottom). The Sun is to the left.

with the plasmapause. The hot tenuous electrons at $L < 3.6$ preexist in the inner magnetosphere. Pitch angle anisotropy A_{rel} (middle panel) increases at L ~4.4–5.5. The bottom panel summarizes the linear and nonlinear growth rates. The MLG rate (black line) is high in the region where the pitch angle anisotropy is high (at L ~4.4–5.5). The nonlinear growth rate for the threshold amplitude at the frequency of the MLG (red line in bottom panel) is also high at L ~4.4–5.3. This indicates that the whistler waves can also grow due to the nonlinear process when waves grow sufficiently in advance due to the linear process. The nonlinear growth rates for the optimum amplitude at the frequency of the MOA (blue line in bottom panel) are high outside the plasmasphere because the hot electron density is high. This implies that the rising-tone chorus waves can be emitted significantly outside the plasmapause (Omura et al., 2013). For Run 2 (the right panels), the linear growth rate is extremely low because of low pitch angle anisotropy (middle panel). While the pitch angle anisotropy is low, the nonlinear growth rates for the optimum amplitude at the frequency of the MOA (blue line in bottom panel) are high outside the plasmapause because the hot electron density is high.

4. Discussion

From these simulation results, we can draw three inferences. First, the whistler-mode waves can grow first in a specific region in the premidnight-postnoon region outside the plasmapause due to the linear mechanism, followed by the nonlinear growth. Second, the whistler waves grow more efficiently over wider areas under the fast solar wind condition because of deep penetration of hot electrons and the large contraction of the plasmasphere. Third, the chorus waves grow nonlinearly in the premidnight-postnoon region outside the plasmapause for the slow solar wind condition, if coherent whistler waves coming from external sources are present in the equatorial plane (Omura et al., 2013).

Regarding the first inference, the following processes can occur in a specific region in the premidnight-postnoon region outside the plasmapause. (1) The whistler waves grow first due to the linear mechanism. (2) When the wave amplitude exceeds the threshold amplitude, further growth can take place due to the nonlinear mechanism (Omura et al., 2009). (3) When the wave amplitude exceeds the optimum amplitude, the nonlinear wave growth saturates, and the wave amplitude decreases, forming a subpacket with a rising tone. (4) The nonlinear wave growth process is repeated at progressively higher frequencies, resulting in a rising-tone chorus element (Omura et al., 2019; Omura & Nunn, 2011). These nonlinear processes are well demonstrated by simulations (Shoji & Omura, 2013). Simulation results taking into account the linear growth only may underestimate the growth of the whistler-mode waves significantly.

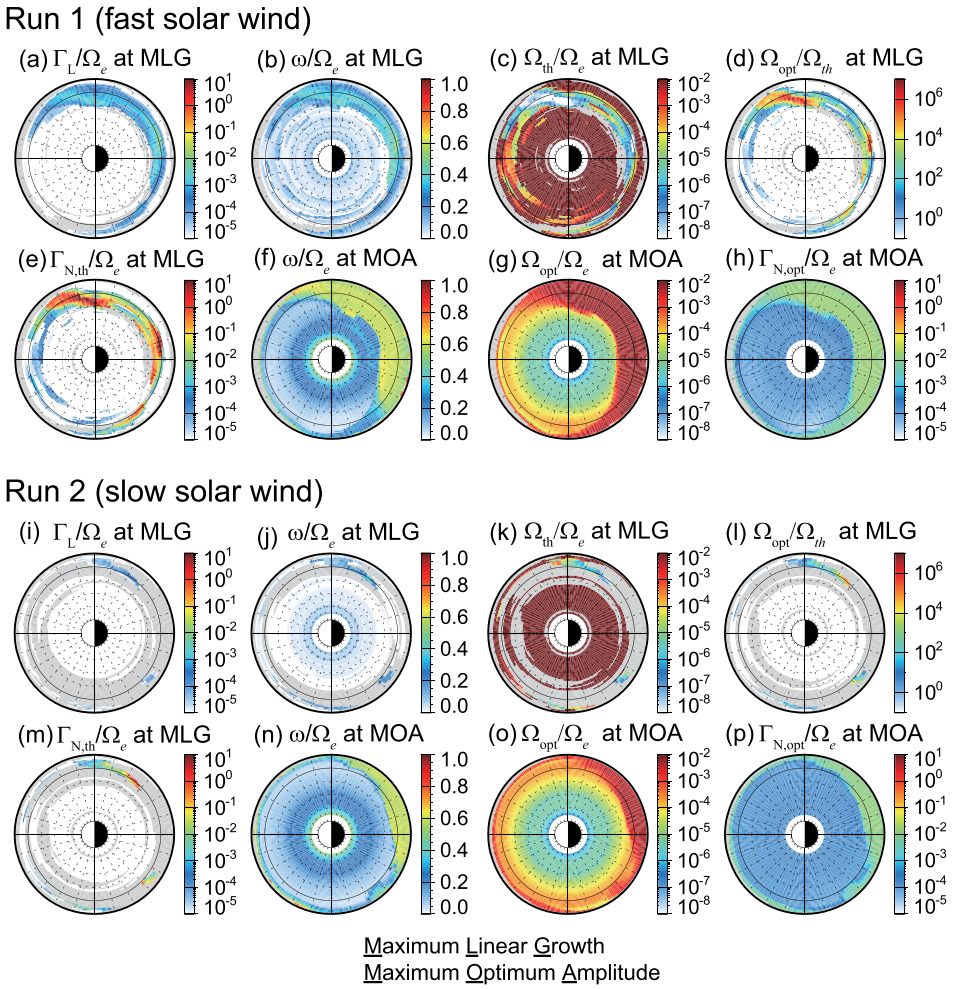

Figure 4. (a, i) Maximum linear growth (MLG) rate normalized to local cyclotron frequency Γ_L/Ω_e, (b, j) normalized wave frequency ω/Ω_e at MLG, (c, k) threshold wave amplitude at MLG, (d, l) ratio of optimum amplitude to threshold amplitude at frequency of MLG, (e, m) normalized nonlinear growth rate for threshold amplitude $\Gamma_{N,th}/\Omega_e$ at frequency of MLG, (f, n) normalized wave frequency ω/Ω_e at maximum optimum amplitude (MOA), (g, o) optimum wave amplitude at frequency of MOA, and (h, p) normalized nonlinear growth rate for optimum amplitude $\Gamma_{N,opt}/\Omega_e$ at frequency of MOA in the equatorial plane at $T = 90$ min for Runs 1 (top) and 2 (bottom).

The second inference may be related to the observations that the averaged electron flux measured at geosynchronous orbit increases with the solar wind speed (Baker & Mcpherron, 1990; Kellerman & Shprits, 2012; Paulikas & Blake, 1979). When the averaged IMF B_z is negative in the fast solar wind stream, the electron flux is shown to increase (Miyoshi & Kataoka, 2008). According to the global MHD simulation, when the solar wind speed is high, a large amount of the solar wind kinetic energy is converted to the magnetic energy (Poynting flux) in the mantle region in the high latitude magnetosphere, together with the solar wind magnetic energy (Ebihara et al., 2019). The energy conversion is regarded as a dynamo process in the mantle region, which is associated with the generation of the Region 1 field-aligned current and the convection (Tanaka, 2000). A combination of the enhancement of the convection electric field and the frequent occurrence of substorms may result in the deep penetration of hot electrons into the inner region and the contraction of the plasmasphere (Ebihara & Tanaka, 2013), giving rise to the efficient growth of the waves linearly and nonlinearly.

For the third inference, we note that triggered chorus waves are observed together with precipitation of energetic electrons in relatively weak geomagnetic activities (Foster et al., 1976; Foster & Rosenberg, 1976; Rosenberg et al., 1971). According to statistical studies, the chorus waves are often observed at $L >$ ~5 not only in high geomagnetic activities but also in relatively weak activities, such as the conditions that *AE* is

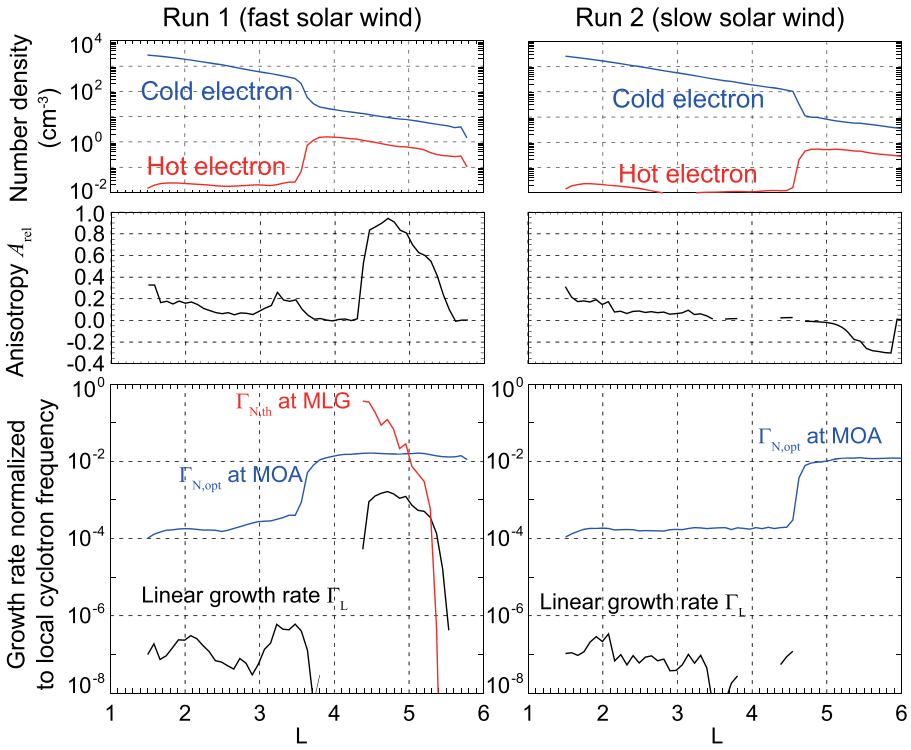

Figure 5. (top) Cold and hot electron densities, (middle) pitch angle anisotropy A_{rel} at wave frequency where the maximum linear growth rate occurs, and (bottom) maximum linear growth rate (black), nonlinear growth rate with threshold amplitude at frequency of MLG (red), and nonlinear growth rate with optimum amplitude at frequency of MOA (blue) at midnight meridian at $T = 90$ min for Runs 1 (left) and 2 (right). The growth rates are normalized to the local cyclotron frequency.

less than 100 (Meredith et al., 2003) and that *AL* is larger than −200 nT (Li et al., 2016). Large-amplitude whistler-mode chorus waves with amplitude >5 mV/m are often observed in the premidnight-postdawn region near the equatorial plane during low geomagnetic activity (*AE* < 300 nT) (Tyler et al., 2019). The simulation results show that for the slow solar wind case, the linear growth is suppressed (Figure 4i), while the nonlinear growth occurs efficiently (Figures 4o and 4p). The calculated *AE* is 320 nT at this moment. This may explain the statistical results in terms of the nonlinear growth that is initiated by the coherent whistler waves coming from other regions.

Coherent elements of the chorus wave are thought to accelerate the electrons efficiently due to the nonlinear processes (Omura et al., 2007; Summers & Omura, 2007). When an amplitude of the chorus wave is relatively high and the wave packet is long-lasting, electrons with energy a few hundreds of kiloelectron volts are immediately accelerated to a few MeV range through relativistic turning acceleration (Omura et al., 2007) and ultrarelativistic acceleration (Summers & Omura, 2007), which occurs when an initial Lorentz factor γ is larger than Ω_{e0}/ω, where Ω_{e0} is the cyclotron frequency in the magnetic equatorial plane. A numerical calculation employing a Green's function method shows the acceleration of electrons quickly and efficiently (Omura et al., 2015). It has also been found that relativistic electrons can be more efficiently accelerated through Landau resonance with obliquely propagating chorus waves (Omura et al., 2019). These efficient acceleration processes may explain reasonably the prompt intensification of relativistic electrons during the substorm interval (Foster et al., 2014).

We have specified the regions where the nonlinear growth of the chorus waves is preferred to occur. The next step is to calculate the interaction with electrons and to evaluate overall impacts of the nonlinear growth of the chorus waves on the electron distributions in the inner magnetosphere. The first attempt has been accomplished by incorporating Green's function method into a test particle simulation (Kubota & Omura, 2018). The bounce-averaged treatment of the Green's function method has been suggested by Omura et al. (2015), which helps implement the method into a global simulation, such as CIMI.

5. Conclusions

Using the global MHD simulation and the advection simulation (CIMI), we calculated linear and nonlinear growth rates and threshold and optimum amplitudes for the nonlinear growth. We reached the following conclusions.

1. In the premidnight-prenoon region outside the plasmapause, the whistler waves can first grow due to the linear mechanism, followed by rapid, nonlinear growth accompanied with rising-tone chorus elements. That is because at the wave frequency of maximum linear growth (MLG), the threshold wave amplitude (at which the nonlinear growth begins) decreases, and the optimum wave amplitude (at which the rising-tone chorus emission occurs) is much larger than the threshold wave amplitude.
2. For the fast solar wind, hot electrons are transported deep earthward, and the plasmasphere is largely contracted. The pitch angle anisotropy and the optimum wave amplitude are high. Because of these reasons, the whistler waves can grow more efficiently due to both the linear and nonlinear mechanisms under the fast solar wind.
3. For the slow solar wind, the linear growth is mostly suppressed, but the nonlinear growth can still take place when some coherent waves coming from external sources are present. This may explain the persistence of dawn chorus and the large-amplitude chorus waves that are often observed in weak geomagnetic activities.

Acknowledgments
The computer simulation was performed on the KDK computer system at the Research Institute for Sustainable Humanosphere, Kyoto University. This study was supported by JSPS KAKENHI grants 15H03732, 15H05815, and 17H06140. The simulation data files and a sample program to read the data files are open to the public at the web (http://space.rish.kyoto-u.ac.jp/paper/2019_nonlineargrowth/).

References

Akasofu, S. I. (1968). *Polar and magnetospheric substorms*. Dordrecht, Holland: D. Reidel Publ. Co.

Albert, J. M. (2002). Nonlinear interaction of outer zone electrons with VLF waves. *Geophysical Research Letters*, *29*(8), 1275. https://doi.org/10.1029/2001gl013941

Baker, D. N., & Mcpherron, R. L. (1990). Extreme energetic particle decreases near geostationary orbit—A manifestation of current diversion within the inner plasma sheet. *Journal of Geophysical Research*, *95*(A5), 6591–6599. https://doi.org/10.1029/JA095iA05p06591

Bortnik, J., Thorne, R. M., & Inan, U. S. (2008). Nonlinear interaction of energetic electrons with large amplitude chorus. *Geophysical Research Letters*, *35*, L21102. https://doi.org/10.1029/2008GL035500

Burtis, W. J., & Helliwell, R. A. (1969). Banded chorus—A new type of VLF radiation observed in the magnetosphere by OGO 1 and OGO 3. *Journal of Geophysical Research*, *74*(11), 3002–3010. https://doi.org/10.1029/JA074i011p03002

Burtis, W. J., & Helliwell, R. A. (1976). Magnetospheric chorus: Occurrence patterns and normalized frequency. *Planetary and Space Science*, *24*(11), 1007–1024. https://doi.org/10.1016/0032-0633(76)90119-7

Cornwall, J. M. (1964). Scattering of energetic trapped electrons by very-low-frequency waves. *Journal of Geophysical Research*, *69*(7), 1251–1258. https://doi.org/10.1029/JZ069i007p01251

Cornwall, J. M., Coroniti, F. V., & Thorne, R. M. (1970). Turbulent loss of ring current protons. *Journal of Geophysical Research*, *75*(25), 4699–4709. https://doi.org/10.1029/JA075i025p04699

Cowley, S. W. H., & Ashour-Abdalla, M. (1976). Adiabatic plasma convection in a dipole field: Electron forbidden-zone effects for a simple electric field model. *Planetary and Space Science*, *24*(9), 805–819. https://doi.org/10.1016/0032-0633(76)90071-4

Davidson, G., & Walt, M. (1977). Loss cone distributions of radiation belt electrons. *Journal of Geophysical Research*, *82*(1), 48–54. https://doi.org/10.1029/JA082i001p00048

Davidson, G. T. (1979). Self-modulated VLF wave-electron interactions in the magnetosphere: A cause of auroral pulsations. *Journal of Geophysical Research*, *84*(A11), 6517. https://doi.org/10.1029/JA084iA11p06517

Davis, T. N., & Sugiura, M. (1966). Auroral electrojet activity index AE and its universal time variations. *Journal of Geophysical Research*, *71*(3), 785–801. https://doi.org/10.1029/JZ071i003p00785

Dungey, J. W. (1963). Loss of Van Allen electrons due to whistlers. *Planetary and Space Science*, *11*(6), 591–595. https://doi.org/10.1016/0032-0633(63)90166-1

Ebihara, Y., & Tanaka, T. (2013). Fundamental properties of substorm time energetic electrons in the inner magnetosphere. *Journal of Geophysical Research: Space Physics*, *118*, 1589–1603. https://doi.org/10.1002/jgra.50115

Ebihara, Y., & Tanaka, T. (2015a). Substorm simulation: Formation of westward traveling surge. *Journal of Geophysical Research: Space Physics*, *120*, 10,466–10,484. https://doi.org/10.1002/2015JA021697

Ebihara, Y., & Tanaka, T. (2015b). Substorm simulation: Insight into the mechanisms of initial brightening. *Journal of Geophysical Research, A: Space Physics*, *120*, 7270–7288. https://doi.org/10.1002/2015JA021516

Ebihara, Y., Tanaka, T., & Kamiyoshikawa, N. (2019). New diagnosis for energy flow from solar wind to ionosphere during substorm: Global MHD simulation. *Journal of Geophysical Research: Space Physics*, *124*, 360–378. https://doi.org/10.1029/2018JA026177

Ebihara, Y., Tanaka, T., & Kikuchi, T. (2014). Counter equatorial electrojet and over shielding after substorm onset: Global MHD simulation study. *Journal of Geophysical Research: Space Physics*, *119*, 7281–7296. https://doi.org/10.1002/2014JA020065

Ejiri, M., Hoffman, R. A., & Smith, P. H. (1980). Energetic particle penetrations into the inner magnetosphere. *Journal of Geophysical Research*, *85*(A2), 653–663. https://doi.org/10.1029/JA085iA02p00653

Ejiri, M. (1978). Trajectory traces of charged particles in the magnetosphere. *Journal of Geophysical Research*, *83*(A10), 4798–4810. https://doi.org/10.1029/JA083iA10p04798

Fok, M.-C., Buzulukova, N. Y., Chen, S.-H., Glocer, A., Nagai, T., Valek, P., & Perez, J. D. (2014). The comprehensive inner magnetosphere-ionosphere model. *Journal of Geophysical Research: Space Physics*, *119*, 7522–7540. https://doi.org/10.1002/2014JA020239

Fok, M.-C., Glocer, A., Zheng, Q., Horne, R. B., Meredith, N. P., Albert, J. M., & Nagai, T. (2011). Recent developments in the radiation belt environment model. *Journal of Atmospheric and Solar-Terrestrial Physics*, *73*(11–12), 1435–1443. https://doi.org/10.1016/j.jastp.2010.09.033

Foster, J. C., Erickson, P. J., Baker, D. N., Claudepierre, S. G., Kletzing, C. A., Kurth, W., et al. (2014). Prompt energization of relativistic and highly relativistic electrons during a substorm interval: Van Allen Probes observations. *Geophysical Research Letters*, *41*, 20–25. https://doi.org/10.1002/2013GL058438

Foster, J. C., & Rosenberg, T. J. (1976). Electron precipitation and VLF emissions associated with cyclotron resonance interactions near the plasmapause. *Journal of Geophysical Research*, *81*(13), 2183–2192. https://doi.org/10.1029/ja081i013p02183

Foster, J. C., Rosenberg, T. J., & Lanzerotti, L. J. (1976). Magnetospheric conditions at the time of enhanced wave-particle interactions near the plasmapause. *Journal of Geophysical Research*, *81*(13), 2175–2182. https://doi.org/10.1029/ja081i013p02175

Hikishima, M., Yagitani, S., Omura, Y., & Nagano, I. (2009). Full particle simulation of whistler-mode rising chorus emissions in the magnetosphere. *Journal of Geophysical Research*, *114*, A01203. https://doi.org/10.1029/2008JA013625

Horne, R. B., & Thorne, R. M. (1998). Potential waves for relativistic electron scattering and stochastic acceleration during magnetic storms. *Geophysical Research Letters*, *25*(15), 3011–3014. https://doi.org/10.1029/98GL01002

Jaynes, A. N., Lessard, M. R., Rodriguez, J. V., Donovan, E., Loto'Aniu, T. M., & Rychert, K. (2013). Pulsating auroral electron flux modulations in the equatorial magnetosphere. *Journal of Geophysical Research: Space Physics*, *118*, 4884–4894. https://doi.org/10.1002/jgra.50434

Jordanova, V. K., Thorne, R. M., Li, W., & Miyoshi, Y. (2010). Excitation of whistler mode chorus from global ring current simulations. *Journal of Geophysical Research*, *115*, A00F10. https://doi.org/10.1029/2009JA014810

Kasahara, S., Miyoshi, Y., Yokota, S., Mitani, T., Kasahara, Y., Matsuda, S., et al. (2018). Pulsating aurora from electron scattering by chorus waves. *Nature*, *554*(7692), 337–340. https://doi.org/10.1038/nature25505

Katoh, Y., & Omura, Y. (2007). Computer simulation of chorus wave generation in the Earth's inner magnetosphere. *Geophysical Research Letters*, *34*, L03102. https://doi.org/10.1029/2006GL028594

Kellerman, A. C., & Shprits, Y. Y. (2012). On the influence of solar wind conditions on the outer-electron radiation belt. *Journal of Geophysical Research*, *117*, A05217. https://doi.org/10.1029/2011JA017253

Kennel, C. F., & Petschek, H. E. (1966). Limit on stably trapped particle fluxes. *Journal of Geophysical Research*, *71*(1), 1–28. https://doi.org/10.1029/JZ071i001p00001

Kubota, Y., & Omura, Y. (2018). Nonlinear dynamics of radiation belt electrons interacting with chorus emissions localized in longitude. *Journal of Geophysical Research: Space Physics*, *123*, 4835–4857. https://doi.org/10.1029/2017JA025050

Kurita, S., Katoh, Y., Omura, Y., Angelopoulos, V., Cully, C. M., Le Contel, O., & Misawa, H. (2012). THEMIS observation of chorus elements without a gap at half the gyrofrequency. *Journal of Geophysical Research*, *117*, A11223. https://doi.org/10.1029/2012JA018076

Li, W., Santolik, O., Bortnik, J., Thorne, R. M., Kletzing, C. A., Kurth, W. S., & Hospodarsky, G. B. (2016). New chorus wave properties near the equator from Van Allen Probes wave observations. *Geophysical Research Letters*, *43*, 4725–4735. https://doi.org/10.1002/2016GL068780

Lyons, L. R. (1974). Pitch angle and energy diffusion coefficients from resonant interactions with ion-cyclotron and whistler waves. *Journal of Plasma Physics*, *12*(3), 417–432. https://doi.org/10.1017/S002237780002537X

Lyons, L. R., Thorne, R. M., & Kennel, C. F. (1972). Pitch-angle diffusion of radiation belt electrons within the plasmasphere. *Journal of Geophysical Research*, *77*(19), 3455–3474. https://doi.org/10.1029/JA077i019p03455

Meredith, N. P., Horne, R. B., Thorne, R. M., & Anderson, R. R. (2003). Favored regions for chorus-driven electron acceleration to relativistic energies in the Earth's outer radiation belt. *Geophysical Research Letters*, *30*(16), 1871. https://doi.org/10.1029/2003GL017698

Miyoshi, Y., & Kataoka, R. (2008). Flux enhancement of the outer radiation belt electrons after the arrival of stream interaction regions. *Journal of Geophysical Research*, *113*, A03S09. https://doi.org/10.1029/2007JA012506

Nishida, A., Iwasaki, N., & Nagata, T. (1966). The origin of fluctuations in the equatorial electrojet: A new type of geomagnetic variation. *Annales de Geophysique*, *22*(January 1966), 478–484. Retrieved from internal-pdf://nishida_a._22_478_1966_ann._geo-1784369153/Nishida_A._22_478_1966_Ann._Geo.pdf

Nishimura, Y., Bortnik, J., Li, W., Thorne, R. M., Lyons, L. R., Angelopoulos, V., et al. (2010). Identifying the driver of pulsating aurora. *Science*, *330*(6000), 81–84. https://doi.org/10.1126/science.1193186

Nunn, D. (1974). A self-consistent theory of triggered VLF emissions. *Planetary and Space Science*, *22*(3), 349–378. https://doi.org/10.1016/0032-0633(74)90070-1

Omura, Y., Hikishima, M., Katoh, Y., Summers, D., & Yagitani, S. (2009). Nonlinear mechanisms of lower-band and upper-band VLF chorus emissions in the magnetosphere. *Journal of Geophysical Research*, *114*, A07217. https://doi.org/10.1029/2009JA014206

Omura, Y., Hsieh, Y., Foster, J. C., Erickson, P. J., Kletzing, C. A., & Baker, D. N. (2019). Cyclotron acceleration of relativistic electrons through Landau resonance with obliquely propagating whistler-mode chorus emissions. *Journal of Geophysical Research: Space Physics*, *124*, 2795–2810. https://doi.org/10.1029/2018JA026374

Omura, Y., Katoh, Y., & Summers, D. (2008). Theory and simulation of the generation of whistler-mode chorus. *Journal of Geophysical Research*, *113*, A04223. https://doi.org/10.1029/2007JA012622

Omura, Y., Miyashita, Y., Yoshikawa, M., Summers, D., Hikishima, M., Ebihara, Y., & Kubota, Y. (2015). Formation process of relativistic electron flux through interaction with chorus emissions in the Earth's inner magnetosphere. *Journal of Geophysical Research, A: Space Physics*, *120*, 9545–9562. https://doi.org/10.1002/2015JA021563

Omura, Y., & Nunn, D. (2011). Triggering process of whistler mode chorus emissions in the magnetosphere. *Journal of Geophysical Research*, *116*, A05205. https://doi.org/10.1029/2010JA016280

Omura, Y., Nunn, D., & Summers, D. (2013). Generation processes of whistler mode chorus emissions: Current status of nonlinear wave growth theory. In D. Summers, I. R. Mann, D. N. Baker, & M. Schulz (Eds.), *Dynamics of the Earth's Radiation Belts and Inner Magnetosphere* (pp. 243–254). Washington DC: American Geophysical Union. https://doi.org/10.1029/2012GM001347

Omura, Y., Summers, D., & Usui, H. (2007). Relativistic turning acceleration of resonant electrons by coherent whistler-mode waves in a dipole magnetic field. *Journal of Geophysical Research*, *112*(A6), A06236. https://doi.org/10.1029/2006JA012243

Paulikas, G. A., & Blake, J. B. (1979). In W. P. Olson (Ed.), *Effects of the solar wind on magnetospheric dynamics: Energetic electrons at the synchronous orbit*, *Geophysical Monograph Series* (pp. 180–202). Washington, DC: American Geophysical Union. https://doi.org/10.1029/GM021p0180

Roederer, J. G. (1970). *Dynamics of geomagnetically trapped radiation* (Vol. 2). Berlin, Heidelberg: Springer Berlin Heidelberg. https://doi.org/10.1007/978-3-642-49300-3

Rosenberg, T. J., Helliwell, R. a., & Katsufrakis, J. P. (1971). Electron precipitation associated with discrete very-low-frequency emissions. *Journal of Geophysical Research*, *76*(34), 8445–8452. https://doi.org/10.1029/JA076i034p08445

Rosenberg, T. J., Siren, J. C., Matthews, D. L., Marthinsen, K., Holtet, J. A., Egeland, A., et al. (1981). Conjugacy of electron microbursts and VLF chorus. *Journal of Geophysical Research*, *86*(A7), 5819–5832. https://doi.org/10.1029/JA086iA07p05819

Roux, A., & Pellat, R. (1978). A theory of triggered emissions. *Journal of Geophysical Research*, *83*(A4), 1433. https://doi.org/10.1029/JA083iA04p01433

Santolík, O., Gurnett, D. A., Pickett, J. S., Parrot, M., & Cornilleau-Wehrlin, N. (2003). Spatio-temporal structure of storm-time chorus. *Journal of Geophysical Research*, *108*, 1278. https://doi.org/10.1029/2002JA009791

Santolík, O., Gurnett, D. A., Pickett, J. S., Parrot, M., & Cornilleau-Wehrlin, N. (2004). A microscopic and nanoscopic view of storm-time chorus on 31 March 2001. *Geophysical Research Letters*, *31*, L02801. https://doi.org/10.1029/2003GL018757

Shoji, M., & Omura, Y. (2013). Triggering process of electromagnetic ion cyclotron rising tone emissions in the inner magnetosphere. *Journal of Geophysical Research: Space Physics*, *118*, 5553–5561. https://doi.org/10.1002/jgra.50523

Spjeldvik, W. N., & Thorne, R. M. (1975). The cause of storm after effects in the middle latitude *D*-region. *Journal of Atmospheric and Terrestrial Physics*, *37*(5), 777–795. https://doi.org/10.1016/0021-9169(75)90021-5

Summers, D., & Ma, C. (2000). A model for generating relativistic electrons in the Earth's inner magnetosphere based on gyroresonant wave-particle interactions. *Journal of Geophysical Research*, *105*(A2), 2625–2639. https://doi.org/10.1029/1999JA900444

Summers, D., & Omura, Y. (2007). Ultra-relativistic acceleration of electrons in planetary magnetospheres. *Geophysical Research Letters*, *34*, L24205. https://doi.org/10.1029/2007GL032226

Summers, D., Thorne, R. M., & Xiao, F. (1998). Relativistic theory of wave-particle resonant diffusion with application to electron acceleration in the magnetosphere. *Journal of Geophysical Research*, *103*(A9), 20,487–20,500. https://doi.org/10.1029/98JA01740

Tanaka, T. (2000). Field-aligned-current systems in the numerically simulated magnetosphere. *Magnetospheric Current Systems*, *Geophysical Monograph Series*, *Vol*. 118, 53–59, Washington DC: American Geophysical Union.

Tanaka, T., Ebihara, Y., Watanabe, M., Den, M., Fujita, S., Kikuchi, T., et al. (2017). Global simulation study for the time sequence of events leading to the substorm onset. *Journal of Geophysical Research: Space Physics*, *122*, 6210–6239. https://doi.org/10.1002/2017JA024102

Tanaka, T. (2015). Substorm auroral dynamics reproduced by advanced global magnetosphere-ionosphere (M-I) coupling simulation. In *Auroral Dynamics and Space Weather* (pp. 177–190). Hoboken, NJ: John Wiley & Sons, Inc. https://doi.org/10.1002/9781118978719.ch13

Trakhtengerts, V. Y. (1995). Magnetosphere cyclotron maser: Backward wave oscillator generation regime. *Journal of Geophysical Research*, *100*(A9), 17205. https://doi.org/10.1029/95ja00843

Tsurutani, B. T., & Smith, E. J. (1974). Postmidnight chorus: A substorm phenomenon. *Journal of Geophysical Research*, *79*(1), 118–127. https://doi.org/10.1029/JA079i001p00118

Tyler, E., Breneman, A., Cattell, C., Wygant, J., Thaller, S., & Malaspina, D. (2019). Statistical occurrence and distribution of high-amplitude whistler mode waves in the outer radiation belt. *Geophysical Research Letters*, *46*, 2328–2336. https://doi.org/10.1029/2019GL082292

Vette, J. (1991). *The AE-8 trapped electron model environment*. Greenbelt, Maryland: NASA/Goddard Space Flight Center.

Vomvoridis, J. L., Crystal, T. L., & Denavit, J. (1982). Theory and computer simulations of magnetospheric very low frequency emissions. *Journal of Geophysical Research*, *87*(A3), 1473–1489. https://doi.org/10.1029/ja087ia03p01473

Xiao, F., Thorne, R. M., & Summers, D. (1998). Instability of electromagnetic R-mode waves in a relativistic plasma. *Physics of Plasmas*, *5*(7), 2489–2497. https://doi.org/10.1063/1.872932